International Journal of Solids and Structures 49 (2012) 2898–2913

Contents lists available at SciVerse ScienceDirect

International Journal of Solids and Structures

journal homepage: www.elsevier.com/locate/ijsolstr

A crack tip tracking algorithm for cohesive interface element analysis of fatigue delamination propagation in composite materials

Luiz F. Kawashita *, Stephen R. Hallett

Advanced Composites Centre for Innovation and Science (ACCIS), University of Bristol, Bristol BS8 1TR, UK

ARTICLE INFO

Article history:
Received 7 September 2011
Received in revised form 16 February 2012
Available online 5 April 2012

Keywords:
Cohesive
Element
Fatigue
Delamination
Fibre
Composite

ABSTRACT

A novel approach is proposed for the use of cohesive elements in the analysis of delamination propagation in composite materials under high-cycle fatigue loading. The method is applicable to delamination propagation within the Paris-law regime and is suitable for the analysis of three-dimensional structures typical of aerospace applications. The major advantages of the proposed formulation are its complete independence of the cohesive zone length – which is a geometry-dependent parameter – and its relative insensitivity to mesh refinement. This is only possible via the introduction of three nonlocal algorithms, which provide (i) automated three-dimensional tracking of delamination fronts, (ii) an estimation of direction of crack propagation and (iii) accurate and mesh-insensitive integration of strain energy release rate. All calculations are updated at every increment of an explicit time-integration finite element solution, which models the envelopes of forces and displacements with an assumption of underlying constant cyclic loading. The method was implemented as a user-defined subroutine in the commercial finite element software LS-Dyna and supports the analysis of complex three-dimensional models. Results are presented for benchmark cases such as specimens with central cut plies and centrally-loaded circular plates. Accurate predictions of delamination growth rates are observed for different mesh topologies in agreement with the Paris-laws of the material.

1. Introduction

Laminated composites are increasingly being used as replacements for metals in safety–critical components for the aerospace industry. The reasons are mainly related to the weight savings that composites can provide over their metallic counterparts for similar levels of stiffness and strength. Another key advantage is the highly anisotropic behaviour of composite laminae which can be used to tailor the in-plane properties of the laminate and provide optimised designs with significant improvements in performance.

Delamination is the mode of failure that requires the lowest load for initiation in laminated composites. During operational conditions, delamination initiation can be facilitated by the presence of manufacturing defects such as voids, fibre waviness, contaminants and others. A delaminated composite will present stiffness changes which, if not directly detrimental to in-service performance, can trigger further damage mechanisms which will result in loss of load bearing capacity.

The susceptibility to delamination often makes safe-life designs impractical for laminated composites. Better solutions are usually obtained via damage-tolerant approaches. The latter require knowledge of the propagation behaviour of flaws under typical operational conditions. Inspection or monitoring techniques are required to estimate the remaining life of the component based either on the characteristics of detectable flaws or by assuming the presence of flaws which are below the detection limits. However, the accurate lifting of composite structures in the presence of delaminations is still a challenge, especially due to the lack of appropriate analysis tools.

The present work addresses the problem of predicting delamination growth in complex laminated structures subjected to high-cycle fatigue loading. The requirement in this case is not only to provide models that predict delamination growth rate with accuracy, but also to ensure that these models are applicable to realistic three-dimensional geometries. The strategy is based on the use of three-dimensional nonlinear finite element (FE) approximations with a modified cohesive zone modelling (CZM) approach for the analysis of fatigue-driven delamination.

The CZM technique combines the classical fracture mechanics concept of a critical strain energy release rate criterion for crack propagation with the damage mechanics assumption of a zone ahead of the crack tip where a gradual and irreversible loss of material stiffness is observed (Dugdale, 1960; Barenblatt, 1962). This approach is very attractive for modelling fracture processes within the FE analysis framework because it avoids the treatment of singular and oscillatory stress fields which would be observed

* Corresponding author. Address: School of Engineering, Cardiff University, The Parade, CF24 3AA Wales, UK. Tel.: +44 (0) 29 208 75910.
E-mail address: KawashitaL@cardiff.ac.uk (L.F. Kawashita).

0020-7683/$ - see front matter © 2012 Elsevier Ltd. All rights reserved.
http://dx.doi.org/10.1016/j.ijsolstr.2012.03.034

with the assumption of linear elasticity. Pioneering works on FE implementations of the CZM technique include Planas and Elices (1991) and Ortiz and Pandolfi (1999) while application to the modelling of delamination in fibre-reinforced composites include Petrossian and Wisnom (1998), Chen et al. (1999), Alfano and Crisfield (2001), Camanho et al. (2003), Borg et al. (2004) and Jiang et al. (2007).

More recently the CZM approach has been further developed to model fatigue crack growth (Nguyen et al., 2001; Yang et al., 2001) and delamination propagation in composites under fatigue loading (Robinson et al., 2005; Turon et al., 2007; Harper and Hallett, 2010). Whilst the advantages of the CZM approach are preserved for the fatigue case, complications arise in the computation of a local damage rate which satisfies the global Paris-law. One limitation, which has been reported elsewhere (Turon et al., 2007; Harper and Hallett, 2010) and will be explored in detail in this paper, is the need for estimating the cohesive zone length ahead of the numerical crack tip. As this length is dependent on the geometry and loading configuration (Harper and Hallett, 2008), the need for its estimation limits the applicability of these models in complex three-dimensional problems.

In this paper an updated method is proposed for modelling fatigue delamination growth in the Paris regime using cohesive interface elements. The methodology eliminates the dependency on the cohesive zone length, which is observed in other formulations reported in the literature, via the automated tracking of numerical delamination fronts. This procedure allows the introduction of further improvements which would not be possible otherwise, namely the computation of effective cohesive element lengths and a more accurate extraction of the strain energy release rate amplitude.

This paper is organised as follows. Section 2 reviews the baseline mixed-mode cohesive formulations for monotonic and cyclic loading. Section 3 describes the proposed enhancements which are related to the use of a crack tip tracking algorithm. In Section 4 two test cases are analysed to illustrate the proposed formulation, and Section 5 summarises the main conclusions of the present work.

2. Cohesive formulation

The cohesive formulations described here have been implemented in the form of 8-node three-dimensional elements with single integration point in the commercial software LS-Dyna, via the addition of a user-defined material subroutine for the under-integrated hexahedral continuum element. This model builds upon the implementation for monotonic loading presented by Li et al. (2008) and extended to fatigue loading by Harper and Hallett (2010).

The displacements of the two surfaces making the cohesive element are interpolated linearly from nodal values at a central integration point so that the resultant displacement jump vector, $\boldsymbol{\delta}$, can be obtained as shown in Fig. 1. The projection of this vector onto one of the surfaces gives three orthogonal displacement components, namely δ_{33}, δ_{12} and δ_{13}. These components represent the cohesive displacements in the out-of-plane, in-plane transverse and in-plane longitudinal directions respectively, following conventional composites notation. Because a resultant shear formulation will be used, the in-plane orientation of the local 1-axis is irrelevant, and the distinction between two shear components δ_{12} and δ_{13} is only required for the finite element implementation.

2.1. Displacement-based damage

In standard cohesive element formulations the degradation of the interface is characterised by the loss of cohesive stiffness which

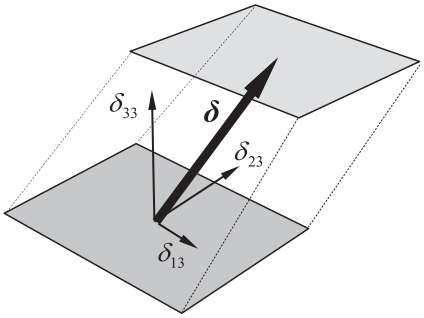

Fig. 1. Displacement components of a cohesive element.

is represented by a scalar damage variable (Chen et al., 1999; Alfano and Crisfield, 2001; Camanho et al., 2003). This variable will be referred to as the static displacement-based damage, D_s, which is a function of the displacement jump across the interface. This variable can be interpreted as the overall macroscopic stiffness loss of the material as a combination of all irreversible micro-structural changes that occur during straining.

The formulation of the displacement-based damage variable utilised in this work has been described elsewhere (Jiang et al., 2007) and is summarised here for completion. The mixed-mode cohesive displacement δ_m is defined in terms of mode-I (opening) and resultant mode-II (shear) components, i.e.,

$$\delta_{\mathrm{I}} = \langle \delta_{33} \rangle, \tag{1}$$

$$\delta_{\mathrm{II}} = \sqrt{\delta_{12}^2 + \delta_{13}^2}, \tag{2}$$

$$\delta_m = \sqrt{\delta_{\mathrm{I}}^2 + \delta_{\mathrm{II}}^2}, \tag{3}$$

where $\langle \cdot \rangle$ is the McCauley bracket, i.e. $\langle \cdot \rangle = \max(\cdot, 0)$.

The cohesive law adopted here is the bilinear model shown in Fig. 2a. For an arbitrary mode ratio, the basic parameters defining the traction-separation response are the cohesive stiffness K, the cohesive strength $\sigma_m^{\max}$ and the critical strain energy release rate G_{C}. The latter is equivalent to the work done per unit area upon complete interface degradation and is given by the integration of cohesive tractions as functions of the displacement jump,

$$G_{\mathrm{C}} = \int_0^{\delta_m^f} \sigma_m \mathrm{d}\delta_m, \tag{4}$$

where σ_m is the mixed-mode traction and δ_m^f is the displacement at failure. G_{C} can be interpreted graphically as the area under the traction-displacement curve in Fig. 2a.

The mixed-mode quantities K, $\sigma_m^{\max}$ and G_{C} are *effective* values which depend on mode ratio. The basic cohesive properties are therefore defined separately for pure modes I and II as shown in Fig. 2b. The effective mixed-mode cohesive law is then calculated

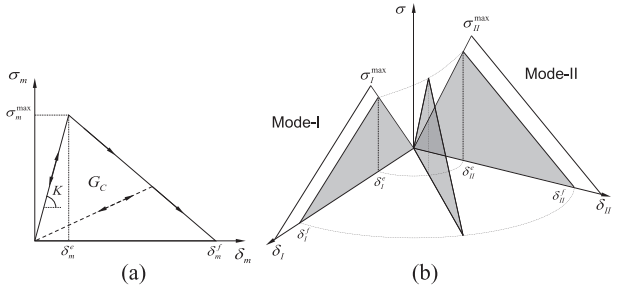

Fig. 2. Mixed-mode cohesive law (a) and its definition in terms of mode-I and mode-II components (b).

and updated at every time increment based on the instantaneous ratio between the cohesive displacements δ_I and δ_{II}, following the formulation described in detail in Jiang et al. (2007).

For initiation a quadratic damage initiation criterion applies,

$$\sqrt{\left(\frac{\langle\sigma_I\rangle}{\sigma_I^{max}}\right)^2+\left(\frac{\sigma_{II}}{\sigma_{II}^{max}}\right)^2}=1, \tag{5}$$

and for failure a linear criterion is used,

$$\frac{G_I}{G_{IC}}+\frac{G_{II}}{G_{IIC}}=1. \tag{6}$$

The displacement-based damage parameter D_s is defined in terms of the resultant cohesive displacements, i.e.,

$$D_s=\frac{\langle\delta_m^{max}-\delta_m^e\rangle}{\delta_m^f-\delta_m^e}, \tag{7}$$

where δ_m^e is the resultant displacement for damage initiation, and δ_m^{max} is the historical maximum resultant displacement given by,

$${}^t\delta_m^{max}=\max({}^{t-\Delta t}\delta_m^{max},{}^t\delta_m), \tag{8}$$

with superscripts ^{t} and $^{t-\Delta t}$ indicating the current and the previous time increments, respectively.

It follows that the interface is undamaged when $D_s=0$, damaged when $0<D_s<1$ and failed when $D_s=1$.

A modification of the formulation above was proposed by Li et al. (2008) which takes into account the enhancement in effective mode-II properties when the interface is under through-thickness compressive stresses. The effective mode-II strength is given by,

$$\overline{\sigma}_{II}^{max}=\sigma_{II}^{max}-\eta\sigma_{33}, \tag{9}$$

where σ_{33} is the through-thickness stress, σ_{II}^{max} is the mode-II delamination strength in the absence of through-thickness stresses, and η is the empirically derived enhancement factor. It is assumed that the initial cohesive stiffness and softening slope remain unchanged with this enhancement. The effective critical mode-II strain energy release rate is then,

$$\overline{G}_{IIC}=\left(1-2\eta\left(\frac{\sigma_{33}}{\sigma_{II}^{max}}\right)+\eta\left(\frac{\sigma_{33}}{\sigma_{II}^{max}}\right)^2\right)G_{IIC}. \tag{10}$$

Li et al. (2008) showed that the experimental results for glass-fibre/epoxy laminates presented by Cui et al. (1994) are best fit with an average value of $\eta=0.74$, which also gives a good fit for high rate tests on carbon-fibre/epoxy specimens. This value has been used in the analysis of cut-ply specimens as will be shown later.

2.2. Fatigue-based damage

When modelling fatigue damage accumulation and propagation over large numbers of cycles, it is often impractical to analyse each load cycle individually. For constant amplitude loading, one alternative is to analyse only the envelopes of forces and displacements (Robinson et al., 2005; Turon et al., 2007; Harper and Hallett, 2010), as illustrated in Fig. 3, using an external variable to represent the number of elapsed load cycles. For explicit time-integration analyses it is convenient to take the number of cycles to be proportional to simulation time. The latter is treated as pseudo-time since it is no longer related to physical properties such as kinetic energy or strain rate.

For the generalised load-controlled problem in Fig. 3 the force applied to the model is initially increased gradually from zero to the desired peak value using a smooth polynomial curve to minimise any dynamic effects. Once the system is in static equilibrium, the fatigue degradation law is activated. This will result in fatigue crack growth and reduction of overall stiffness, causing the displacement envelopes to expand as shown in Fig. 3. During a fatigue analysis, changes to the boundary conditions (e.g. changes in load amplitude) must be gradual since the solution should not be affected by dynamic effects.

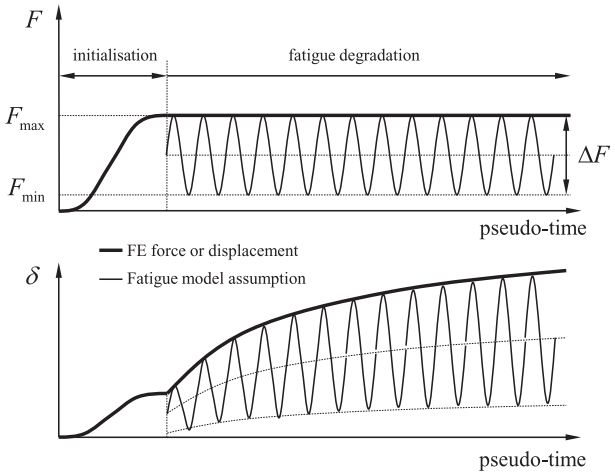

Fig. 3. Modelling the envelopes of loads and displacements in a cyclic regime.

The underlying formulation for propagation of a delamination under cyclic loading follows that of Harper and Hallett (2010) which uses a modified Paris-law,

$$\frac{da}{dN}=C\left(\frac{\Delta G}{G_C}\right)^m, \tag{11}$$

where a is the delamination length, N is the number of load cycles, ΔG is the strain energy release rate amplitude, G_C is the mixed-mode critical strain energy release rate (see Eq. (4)), and C and m are empirical parameters derived from experimental data. For load-controlled tests the strain energy release rate amplitude ΔG is obtained from the peak value of strain energy release rate, G_{max}, via,

$$\Delta G=(1-R^2)G_{max}, \tag{12}$$

where R is the positive and constant ratio between trough and peak applied loads (*R-ratio*).

In order to account for the accumulation of damage during cyclic loading, a fatigue damage parameter D_f is introduced (following Robinson et al. (2005)) so that the total accumulated damage becomes,

$$D_{tot}=D_s+D_f. \tag{13}$$

The computation of the fatigue component D_f requires several steps. Firstly, the peak value of strain energy release rate, G_{max}, is obtained for each cohesive integration point via the numerical integration of the history of tractions and displacements at that point, i.e. evaluating Eq. (4) in discrete form. We use a midpoint rule so that at a given time step t the instantaneous value of the integrated strain energy release rate is,

$$G_{max}^{(inst)}=\sum_{k=1}^{nstep(t)}\left(\frac{\sigma_k+\sigma_{k-1}}{2}\right)(\delta_k-\delta_{k-1}), \tag{14}$$

where k is the increment number and nstep (t) is the number of increments between time zero and time t.

Previous implementations of fatigue cohesive elements reported in the literature (Robinson et al., 2005; Turon et al., 2007; Harper and Hallett, 2010) used instantaneous values of strain energy release rate to compute the fatigue degradation rate, i.e. assuming that $G_{max}=G_{max}^{(inst)}$. It will be shown that $G_{max}^{(inst)}$ can vary considerably during the fatigue degradation of a cohesive element,

so an alternative definition for G_{max} is proposed in the present work.

Once ΔG is known, a local measure of delamination growth rate, da/dN, can be computed using the modified Paris-law in Eq. (11). This delamination growth rate must then be converted into a fatigue damage rate, dD_f/dN, to be used in the constitutive update of the cohesive element.

This conversion requires knowledge of the area within the cohesive zone where fatigue damage is being accumulated. Previous work on fatigue cohesive elements (Turon et al., 2007; Harper and Hallett, 2010) performed the computation of D_f at every integration point within the cohesive zone, and by doing so required an estimation of the cohesive zone length in the direction of propagation. Because the cohesive zone length is a load and geometry-dependent parameter (Turon et al., 2008; Harper and Hallett, 2008), the present work aimed at developing a formulation which is independent of this value and of any assumptions required for its estimation. This makes the model more appropriate for use in arbitrary three-dimensional geometries with complex loading conditions.

Here the damage rate is derived in terms of an effective element length l_e which represents the length associated with a single cohesive integration point in the direction of crack propagation. This length is obtained from nodal coordinates as will be discussed in Section 3.2. According to the Paris-law in Eq. (11), the delamination will advance the distance l_e after a certain number of cycles to failure, ΔN_e, has elapsed so that,

$$\Delta N_e = \frac{dN}{da} l_e. \tag{15}$$

Therefore ΔN_e is the number of cycles within which the cohesive element of length l_e must fail due to fatigue damage accumulation, as dictated by the input Paris-law.

The fatigue damage parameter D_f is updated at every time step according to the computed fatigue damage rate dD_f/dN. This rate is a function of the current state of cohesive displacements at the integration point, which is represented by D_s. If the additional damage required to cause point-wise failure is $\Delta D = 1 - D_s$, then the fatigue damage rate can be defined as,

$$\frac{dD_f}{dN} = \frac{\Delta D}{\Delta N_e} = \frac{1 - D_s}{\Delta N_e}. \tag{16}$$

The updated fatigue damage parameter at time t is finally,

$${}^{t}D_f = {}^{t-\Delta t}D_f + \frac{dD_f}{dN}\frac{dN}{dt}\Delta t, \tag{17}$$

where ${}^{t-\Delta t}D_f$ is the fatigue damage variable at the previous time increment and dN/dt is the user-defined loading frequency which can be defined as an arbitrary curve in pseudo-time, i.e. $dN/dt = f(t)$.

It should be noted that Eqs. (15)–(17) are evaluated (in this order) at every increment of the explicit solution. Therefore any changes to the displacement-driven damage variable are immediately taken into account during a fatigue analysis. Moreover, the pure displacement-based cohesive model can be retrieved at any time by setting the loading frequency $f(t)$ to zero. These features enable the analysis of complex load cases including variable load amplitude, fatigue degradation leading to unstable propagation, and the determination of residual strength after fatigue. The key contributions of the present work are however related to an increased accuracy in the evaluation of Eq. (15). As will be shown in Section 3, the effective length l_e can be computed automatically, and the crack growth rate da/dN determined more accurately with the use of a crack tip tracking algorithm.

The degradation of cohesive tractions due to the presence of fatigue damage is illustrated by the traction-damage curve in Fig. 4. At time t_0 the interface has accumulated displacement-based damage only, and at time $t_0 + \Delta t$ the first fatigue degradation occurs. Cohesive stresses are then evaluated from the total damage variable D_{tot}, reducing the cohesive traction to a point below the original softening curve.

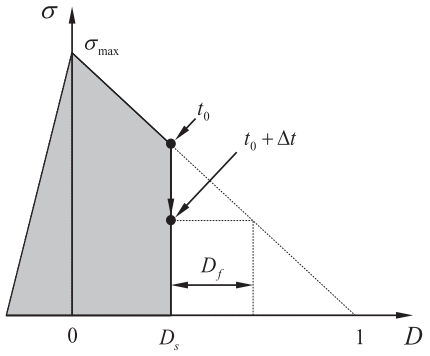

Fig. 4. Stress-damage curve showing degradation due to fatigue damage.

The presence of a fatigue damage component D_f causes the global stiffness of the interface to decrease, resulting in a further increase in relative displacements. Therefore the displacement-based damage variable D_s also increases when fatigue damage is accumulated, as shown in Fig. 5a (Harper and Hallett, 2010). This will cause the instantaneous measure of strain energy release rate, $G_{max}^{(inst)}$, to increase as the element undergoes fatigue degradation, as shown by the shaded area in Fig. 5a. The total work per unit area for crack propagation under this combination of displacement-based and fatigue-based damage is $G_{max}^{(fail)}$, which is shown as the shaded area in Fig. 5b.

The procedures above have been described for a constant mode ratio. In order to enable the analysis at any ratio between mode-I and mode-II two options of mixed-mode growth laws have been implemented. The first is a simple linear rule of mixtures between modes I and II, i.e.,

$$C = \frac{G_I}{G_I + G_{II}} C_I + \frac{G_{II}}{G_I + G_{II}} C_{II}, \tag{18}$$

$$m = \frac{G_I}{G_I + G_{II}} m_I + \frac{G_{II}}{G_I + G_{II}} m_{II}, \tag{19}$$

where the subscripts indicate mode-I or mode-II components.

The second option is a more sophisticated non-monotonic rule developed by Blanco et al. (2004) which had been implemented previously by Harper and Hallett (2010), i.e.,

$$\log C = \log C_I + \log C_m \left(\frac{G_{II}}{G_I + G_{II}}\right) + \log \frac{C_{II}}{C_I C_m} \left(\frac{G_{II}}{G_I + G_{II}}\right)^2, \tag{20}$$

$$m = m_I + m_m \left(\frac{G_{II}}{G_I + G_{II}}\right) + (m_{II} - m_I - m_m) \left(\frac{G_{II}}{G_I + G_{II}}\right)^2 \tag{21}$$

where the subscript $_m$ indicates that an additional Paris-law is required at an intermediate mode ratio.

3. Nonlocal algorithms

3.1. Crack tip tracking

Previous work on fatigue cohesive elements (Robinson et al., 2005; Turon et al., 2007; Harper and Hallett, 2010) relied on the application of a fatigue degradation parameter to *every* cohesive integration point within the damage zone, i.e. every cohesive element for which the displacement jump was greater than the displacement for damage initiation. Therefore these formulations were *point-local*, meaning that the state of a cohesive integration point depended solely on the properties of that point alone.

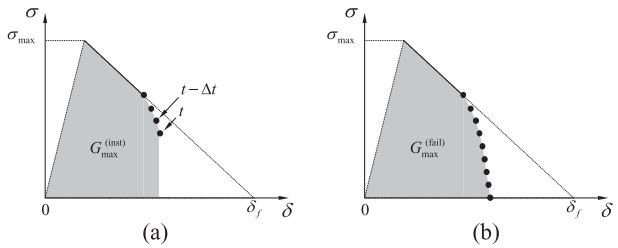

Fig. 5. Different measures of integrated strain energy release rate, (a) instantaneous value at time t and (b) final value at failure.

Point-local algorithms are generally the choice when working with commercial finite element software because most user-defined subroutines are point-local by default.

Computing a fatigue degradation rate for every damaged element within the cohesive zone adds a further level of complexity to the analysis when the phenomenological Paris-law is employed. More specifically, the conversion of the point-local strain energy release rate amplitude into the correct macroscopic crack growth rate will require knowledge of the cohesive zone length in the direction of crack propagation.

Turon et al. (2007) proposed the use of a closed form analytical solution for mode-I loading of a Double Cantilever Beam (DCB) specimen to estimate the ratio between the element area and the total area of the cohesive zone. Although this method was shown to predict fairly well also mode-II and mixed-mode fatigue delamination, its accuracy for full three-dimensional geometries will depend on the validity of this assumption regarding the cohesive zone length, which was investigated by Harper and Hallett (2008).

Harper and Hallett (2010) opted to leave the cohesive zone length as an input parameter to be determined either via analytical solutions or additional finite element analyses. They assumed that the fatigue degradation affected only one half of the cohesive zone length, which provided good agreement with experimental results.

In the present work a new formulation is proposed which is independent of the cohesive zone length and has a considerably lower dependency on mesh refinement, therefore being more appropriate for use in full three-dimensional problems. This formulation is based on the introduction of three nonlocal aspects in the computation of fatigue damage rate, namely:

- identification and tracking of cohesive elements pertaining to delamination fronts;
- estimation of the local direction of crack propagation and the computation of effective element lengths;
- computation of crack growth rate based on the integrated strain energy release rate at failure.

The implementation was done in the commercial software LS-Dyna but is general enough so that it can be ported to other commercial explicit FE solvers as long as user-defined element subroutines are available. The implementation is based on a user-defined constitutive law for cohesive elements plus separate algorithms for the nonlocal computations described above. The latter were compiled together with the user-defined constitutive subroutine but were called only once at every new time step. This allowed the nonlocal algorithms to interact with the constitutive update with virtually no interruption to the solution process, and therefore negligible increase in CPU usage.

The crack tip tracking algorithm performs an initial search for potential delamination fronts at the start of the fatigue loading step. This search is based on the analysis of local maxima in instantaneous strain energy release rate, $G^{(\mathrm{inst})}_{\mathrm{max}}$. Elements with high local $G^{(\mathrm{inst})}_{\mathrm{max}}$ are identified as potential delamination fronts and will accumulate fatigue damage. This initial search avoids the need for pre-existing cracks, and ensures that multiple delaminations are taken into account.

Once the fatigue degradation has been activated, the tracking of crack fronts is accomplished via the exchange of point-local data between neighbouring integration points whenever a cohesive failure occurs. Once an element fails its immediate neighbours are marked as being part of the new delamination front, effectively tracking this front as it propagates in any direction.

The advantage of using such a tracking procedure is that the fatigue-driven damage D_f can be computed exclusively for cohesive elements at the crack tip. In this way the reference length l_e in Eq. (15) becomes a function of the element dimensions only and knowledge of the cohesive zone length is no longer required.

The crack tip tracking procedure is illustrated in Fig. 6. For the baseline formulation, Paris-law degradation is introduced whenever a cohesive element enters the inelastic regime, so it will affect all elements within the cohesive zone. In this case the only available measure of strain energy release rate is the point-local value of $G^{(\mathrm{inst})}_{\mathrm{max}}$. On the other hand, when the crack tip tracking algorithm is used, the computation of fatigue damage can be restricted to the cohesive elements at the numerical crack tip. In this case other measures of strain energy release rate can be used as will be shown later.

3.2. Direction of propagation and effective element length

The modified Paris curve in Eq. (11) defines a one-dimensional crack growth rate. In order to reproduce this growth accurately in three dimensions, the length l_e in Eq. (15) must reflect the effective contribution of that cohesive integration point to the advancement of the crack. Because the cohesive elements cover quadrilateral areas of the interface, the effective length l_e will be a function of the in-plane direction of crack propagation. Variations in effective lengths are especially noticeable when the cohesive elements have large aspect ratios.

The solution proposed in this work consists of a nonlocal algorithm that estimates the direction of propagation for each cohesive element along the crack front. This is done based on the analysis of its neighbouring elements at every time increment. The effective element length is taken as the distance between consecutive 'rows' of integration points assuming that the pattern observed at the current element is repeated over its nearest neighbours. In order to minimise the computational overhead, only the four nearest neighbours of each cohesive element are included in the check. This results in five possible directions of propagation for each quadrant as shown in Fig. 7. The five values of l_e are shown graphically in Fig. 7 together with their expressions in terms of the two in-plane *average* lengths l_1 and l_2, which are obtained via the interpolation of nodal coordinates.

For minimisation of CPU cost, these five effective lengths are pre-computed at the start of the fatigue degradation step and stored as state variables for each cohesive element in the model. The choice of which length is used for the calculation of fatigue damage rate is made on-the-fly according to the state of the nearest neighbours at the current time step.

Clearly this algorithm will produce only coarse estimates of the direction of crack propagation but as will be shown in later sections, it seems to provide a good balance between CPU cost and accuracy, effectively removing the mesh bias otherwise seen with elements of large aspect ratio.

3.3. Strain energy release rate extraction

As mentioned earlier, the instantaneous measure of strain energy release rate $G^{(\mathrm{inst})}_{\mathrm{max}}$ varies as the elements accumulate fatigue

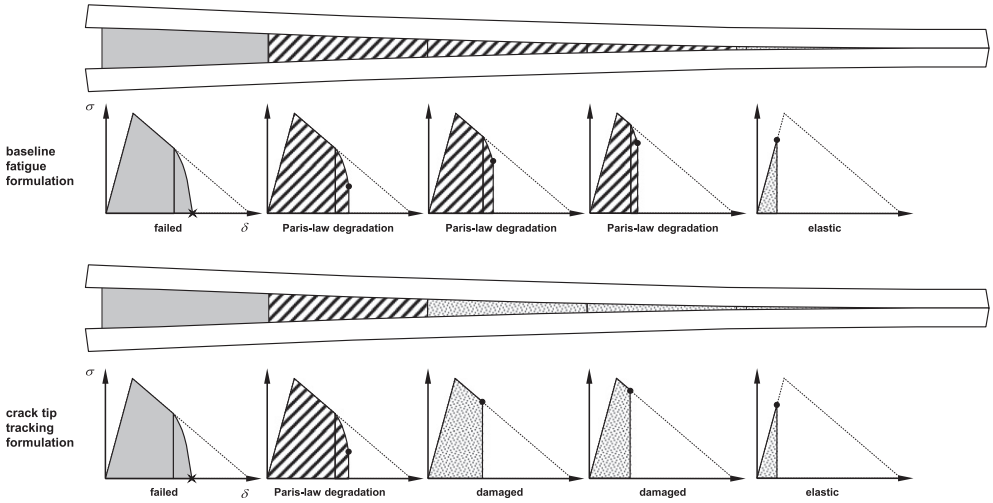

Fig. 6. Application of fatigue damage without and with the crack tip tracking algorithm.

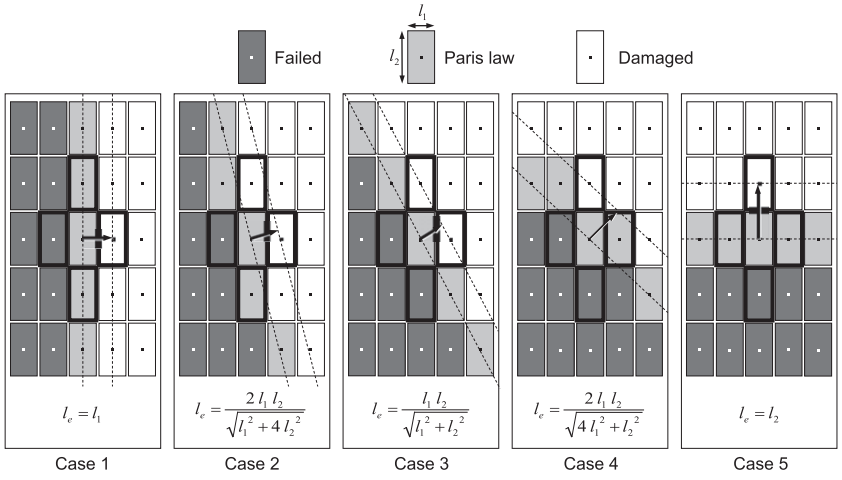

Fig. 7. Five effective in-plane element lengths (in each quadrant) for a given cohesive element (at the numerical crack tip) based on the status of its four nearest neighbours.

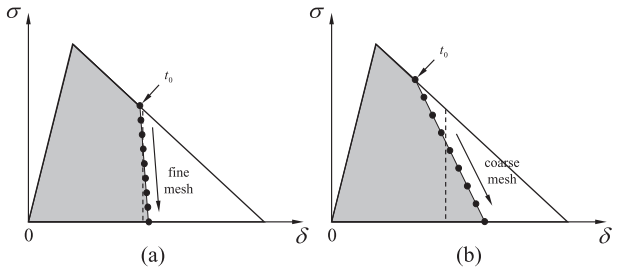

Fig. 8. Fatigue degradation at the crack tip cohesive element for (a) a fine mesh and (b) a coarse mesh (the dashed line shows the ideal behaviour for $l_e \to 0$).

damage. Moreover, the magnitude of the variation in $G_{\max}^{(\text{inst})}$ with increasing fatigue damage depends on the level of mesh refinement, being more pronounced in coarser meshes. Fig. 8 illustrates this phenomenon for two different levels of mesh refinement. In fine meshes, Fig. 8a, the high resolution of the cohesive zone results in an accurate measure of D_s at the crack tip at time t_0. The dashed line shows the ideal traction-separation behaviour for an ideal mesh where $l_e \to 0$. Because the element area is small, its contribution to the overall interfacial stiffness is also small and during fatigue degradation, i.e. for $t > t_0$, the cohesive displacements will increase only slightly so that $G_{\max}^{(\text{inst})}$ will remain nearly constant. On the other hand, for coarse meshes, Fig. 8b, the resolution of the cohesive zone is poor and D_s is under-estimated at the crack tip at time t_0. Because the element is large, it will have a more significant contribution the overall interfacial stiffness. Therefore, during fatigue degradation the cohesive displacements will increase considerably causing a noticeable increase in $G_{\max}^{(\text{inst})}$.

The variable nature of $G_{\max}^{(\text{inst})}$ with fatigue degradation and mesh refinement make it an inappropriate measure of strain energy release rate for the translation of the Paris-law into an element damage rate. Instead, one would seek to use the final value, $G_{\max}^{(\text{fail})}$, which is the best estimate of the total energy dissipated during crack propagation over the element area. However, the correct value of $G_{\max}^{(\text{fail})}$ is not available until the element has undergone full fatigue degradation, so it cannot be used to determine how the element should be degraded. Therefore it seems impossible to reproduce the Paris-law accurately using point-local formulations alone. To address this issue, we introduce a third nonlocal aspect in the calculation of fatigue damage rate which is the extraction of the total strain energy release rate at failure, $G_{\max}^{(\text{fail})}$, from elements in the wake of the numerical crack front. This method assumes that the variation of $G_{\max}^{(\text{fail})}$ between consecutive cohesive elements is small, which holds true for the majority of cases of practical interest.

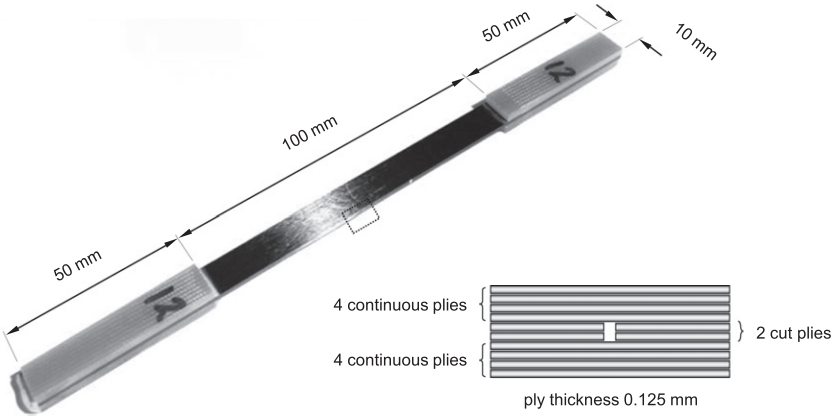

Fig. 9. Cut-ply specimen geometry and detail of the central discontinuous plies.

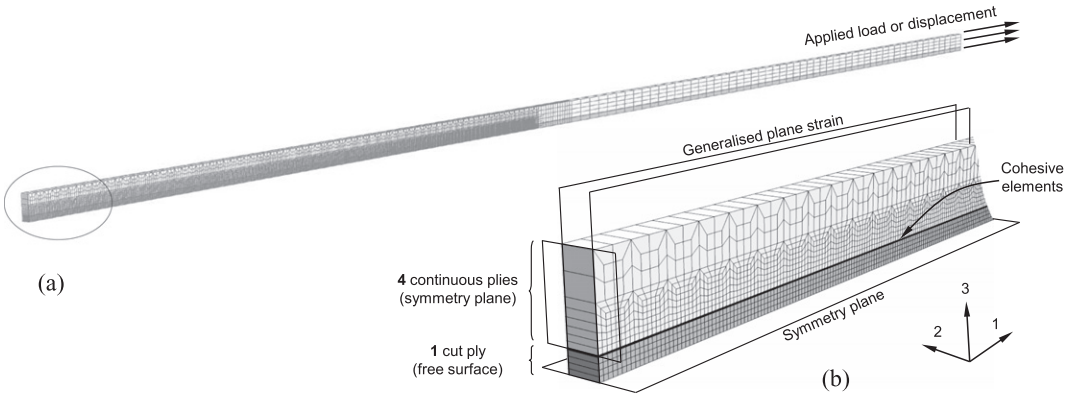

Fig. 10. Finite element model of a cut-ply specimen (quarter model).

Though, as a conservative measure the value of $G_{\max}^{(\text{fail})}$ is used if and only if it is greater than the instantaneous value of $G_{\max}^{(\text{inst})}$ for the current element. The nonlocal integrated strain energy release rate is therefore,

$$G_{\max}^{(\text{NL})} = \max\left(G_{\max}^{(\text{inst})}, G_{\max,1}^{(\text{fail})}, G_{\max,2}^{(\text{fail})}, G_{\max,3}^{(\text{fail})}, \ldots, G_{\max,n}^{(\text{fail})}\right), \tag{22}$$

where the indices represent a subset of n elements used by the nonlocal algorithm, and $G_{\max,i}^{(\text{fail})} = 0$ if the ith neighbour has not yet failed. For the 8-node cohesive elements adopted in the present work only the four nearest neighbours are considered for simplicity.

4. Test cases

Two test cases have been used to demonstrate the formulations described above, namely:

- central cut-ply specimens in tension–tension loading (Allegri et al., 2011), where the mode-II loading and the refined mesh result in a high resolution of the cohesive zone;
- NAFEMS benchmark for circular delamination (Davies, 2002; Davies and Zhang, 1995), here extended to the analysis of fatigue loading, where the three-dimensional aspects of the formulation are explored with variable mesh refinement.

4.1. Cut-ply specimens

The testing and analysis of unidirectional central cut-ply specimens was described in detail by Cui et al. (1994) for glass-fibre/epoxy laminates. The introduction of discontinuous central plies promotes mode-II delamination along four interfaces when longitudinal tensile loads are applied, as shown in Fig. 9.

The experimental data presented here are the result of a recent test programme carried out at the University of Bristol on the Hexcel IM7/8552 carbon/epoxy pre-preg material. Laminates containing eight continuous plies and two central cut plies were manufactured on flat tooling as larger plates and cured in an autoclave. Final cured ply thicknesses were on average 0.125 mm. Glass/epoxy end tabs were adhesively bonded to the plate before individual specimens could be machined to the final dimensions shown in Fig. 9. Tests were performed under quasi-static tension and tension–tension fatigue in a servo-hydraulic testing machine.

4.1.1. Quasi-static loading

Quasi-static tests were performed under a crosshead velocity of 0.5 mm min^{-1}. The average net section failure stress (which takes into account only the thickness of continuous plies) was 1932.3 MPa with a coefficient of variation of 2.1% for five repeats.

A finite element model of the gauge section of the specimen was produced as shown in Fig. 10. Only a quarter model was required due to symmetries. For compatibility with the three-dimensional cohesive elements described in Section 2, 'slice' models were built using hexahedral continuum elements. Only one element was needed along the width direction and a state of *generalised plane strain* was assumed. In relation to the global coordinate system depicted in Fig. 10b, this assumption meant that the strains ε_{22} were constant throughout the model. This was achieved via the introduction of kinematic constraints which enforced zero 2-direction

Table 1
Elastic properties for IM7/8552 UD laminates.

E_{11} [MPa]	E_{22} [MPa]	E_{33} [MPa]	ν_{12}	ν_{13}	ν_{23}	G_{12} [MPa]	G_{13} [MPa]	G_{23} [MPa]	ρ [g cm^{-3}]
161000	11380	11380	0.32	0.32	0.436	5170	5170	3980	1.5

Table 2
Interlaminar cohesive properties for IM7/8552.

G_{IC} [N mm^{-1}]	G_{IIC} [N mm^{-1}]	σ_I^{max} [MPa]	σ_{II}^{max} [MPa]	K_I [N mm^{-3}]	K_{II} [N mm^{-3}]	η
0.2	1.0	60.0	90.0	4.67×10^5	1.75×10^5	0.74

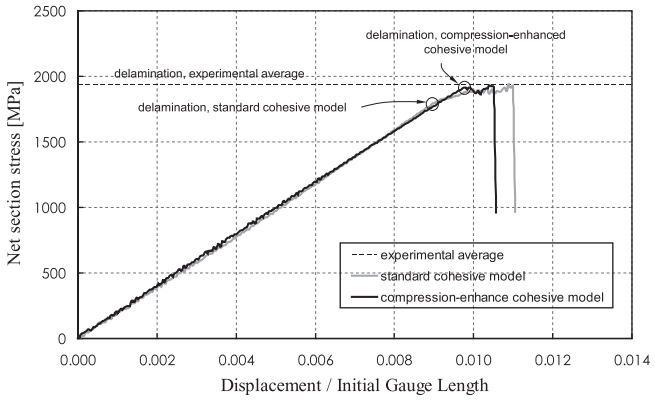

Fig. 11. Numerical and experimental curves of net section stress versus displacement for quasi-static cut-ply tests.

Table 3
Mode-II Paris-law coefficients for unidirectional IM7/8552 laminates obtained from cut-ply tests.

R-ratio	C_{II}	m_{II}
0.1	0.0669	6.37
0.3	0.2094	10.75
0.5	2.2235	20.40

displacements for all nodes on one side of the slice, and coupled 2-direction displacements for all nodes on the other side.

The distinction between continuous and cut plies resided in the definition of boundary conditions for the longitudinal symmetry plane (Fig. 10b). The cross-section of continuous plies was represented by symmetry boundary conditions, while the cross-section of cut plies was left as a free surface. The mesh was refined near the interface between continuous and discontinuous plies for the first 25 mm from the plane of the cut, and coarsened gradually elsewhere. The minimum element length was 0.03125 mm $^1/_4$ of a ply thickness) and the maximum was 0.5 mm, while the width of the model was set to 0.2 mm. User-defined cohesive elements were inserted along the interface, offsetting continuous and discontinuous plies by the interface element thickness of 0.01 mm. In order to reduce the required runtime, the mass was scaled by a factor of 10^5 which resulted in relatively short CPU times while still avoiding excessive dynamic effects. Because these are unidirectional laminates, thermal residual stresses have been neglected.

Elastic material properties for IM7/8552 were obtained from Jiang et al. (2007) and are shown in Table 1. Critical fracture energies for delamination along 0° ply interfaces were obtained from a best fit to experimental mixed-mode data presented by Jimenez and Miravete (2004) and are shown together with the remaining basic cohesive properties in Table 2.

Quasi-static tests were modelled by imposing a displacement boundary condition to all nodes at the end of the gauge section (i.e. 50 mm away from the cut), at a value of 1 mm s^{-1}.

Experimental and numerical results for static loading are compared in Fig. 11. A good agreement is observed in terms of load for first delamination, with a slightly closer agreement for the compression enhanced cohesive formulation, Eqs. (9) and (10), due to the presence of a moderate compressive stress of about 35 MPa across the interface at the delamination load.

The strain energy release rate associated with cut-ply delamination was obtained via the closed-form solution proposed by Petrossian and Wisnom (1998),

$$G = \frac{\sigma_{net}^2 (h_{tot} - h_{cut}) h_{cut}}{4 E_{11} h_{tot}}, \tag{23}$$

where σ_{net} is the average net section stress, h_{tot} is the total specimen thickness, h_{cut} is the thickness of discontinuous plies, and E_{11} is the elastic modulus in the fibre direction. The average strain energy release rate computed from experimental data was 1.18 N mm^{-1}. This is slightly higher than the 1.0 N mm^{-1} input value but should in fact be compared to the enhanced value of 1.247 N mm^{-1} obtained from Eq. (10).

4.1.2. Fatigue loading

During the fatigue experiments, a clip-gauge extensometer was placed over the centre of the gauge length, across the central cut, so that delamination crack growth rates (da/dN) could be estimated from the rate of change in dynamic modulus. Peak forces were chosen as different fractions of the average (net section) static failure stress, namely 75%, 70%, 60%, 50% and 40% severities. Tests were performed with R-ratios of 0.1, 0.3 and 0.5. Loading frequencies were adjusted in order to keep a constant stress rate between all tests, with the baseline frequency being 5 Hz for the 75% severity case. The Paris-law coefficients obtained from cut-ply tests are shown in Table 3.

The analysis of fatigue tests using the envelope modelling technique required the application of a distributed force at the end of the gauge section which was increased gradually from zero to the required peak force before the start of the fatigue degradation step. Analyses were performed with and without the crack tip tracking algorithm and because meshes were fine, only the instantaneous measure of strain energy release rate $G_{max}^{(inst)}$ was used for cut-ply specimens.

The effect of the crack tip tracking algorithm can be seen in Fig. 12 which shows the state of cohesive elements for the 75% severity case at a delamination length of about 0.9 mm. Without crack tip tracking every damaged element accumulates fatigue damage, while with an active tracking only the element nearest to the crack tip is under the Paris-law degradation.

It can be seen from Fig. 12 that the cohesive zone spans a large number of elements in this model. This is a result of the combination of mode-II loading, which in general involves higher toughness

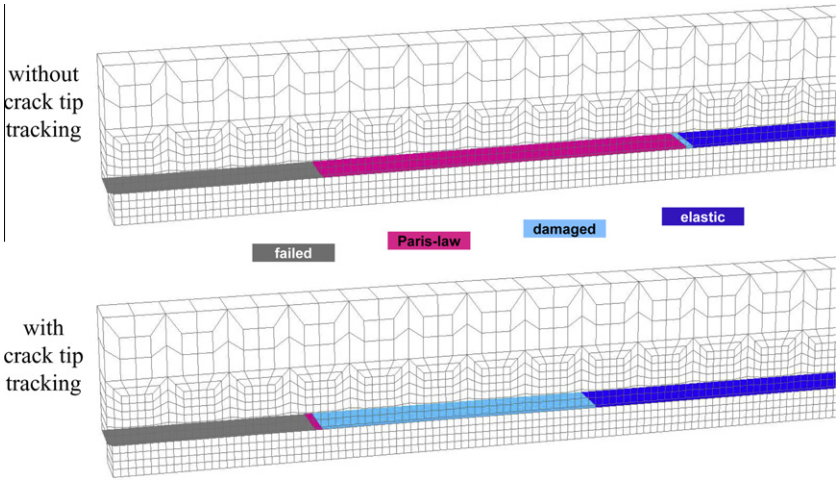

Fig. 12. Cohesive element status for a cut-ply specimen under fatigue, 75% load severity, with a crack length of 0.9 mm.

and consequently longer cohesive zones, and a relatively fine mesh. For the 75% severity case the cohesive zone spanned around 39 elements (1.2 mm) when the tracking was active and around 52 elements (1.6 mm) when the tracking was deactivated. The different lengths reflect the fact that different stress distributions are observed within the cohesive zone with the different formulations. Fig. 13 shows the effective traction-separation curves obtained for a series of cohesive elements in the path of the fatigue crack. Without the crack tip tracking, Fig. 13a, the fatigue traction-separation curves never exactly followed the reference (static) softening curve. With the tracking active, Fig. 13b, the reference curve is followed for a considerable portion of the softening region, up to the point where the elements became part of the numerical crack front, from where rapid fatigue degradation takes place.

Even though the effective traction-separation responses in Figs. 13a and 13b are considerably different, the energies dissipated in each case were very similar. Fig. 14 shows the final strain energy release rates, $G_{max}^{(fail)}$, computed along the crack path for cut-ply specimens with and without the tracking algorithm, for four different values of peak load and a constant R-ratio of 0.1. Analytical solutions using Eq. (23) are also shown for comparison. Numerical strain energy release rates were initially higher than the analytical values because near the cut (i.e. when the cracks are short) extra work is required for the formation of a cohesive zone along an initially pristine interface. Once the delamination had grown about one millimetre away from the initial cut, both formulations predicted nearly identical values of $G_{max}^{(fail)}$ which were also in excellent agreement with the analytical solution.

In order to facilitate the post-processing of numerical results, the number of load cycles to failure was output by the user-defined subroutine for every failed cohesive element. Combining these data with the spatial coordinates of each integration point allowed the construction of effective Paris curves with the predicted crack growth rates. Fig. 15 shows experimental and numerical Paris curves for the R-ratio of 0.1. It can be seen that the crack tip tracking formulation reproduced well the experimental Paris-law as expected. Without the crack tip tracking algorithm however the crack growth rates were considerably overestimated. This was due to the computation of a fatigue damage component for every element within the cohesive zone, based on individual element lengths l_e, without any correction for the cohesive zone length. As the overestimation in delamination growth rate is dependent on the length of the cohesive zone, the numerical Paris curves without crack tip tracking show a different slope when compared with the theoretical curve.

For completeness, the two other R-ratios used in the experimental programme, 0.3 and 0.5, were also analysed with the crack tip tracking model and the results are summarised in Fig. 16. Excellent agreement is observed between the input Paris curves and the effective crack growth rates as expected.

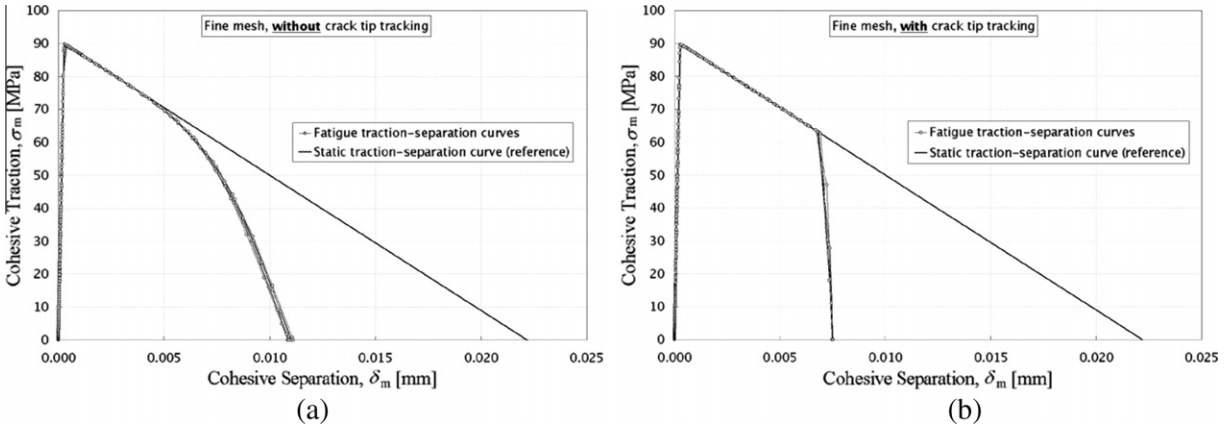

Fig. 13. Traction-separation histories for the cut-ply specimen model, (a) without and (b) with crack tip tracking (fine mesh, data sampled in 1 mm intervals starting 2 mm away from the ply discontinuity).

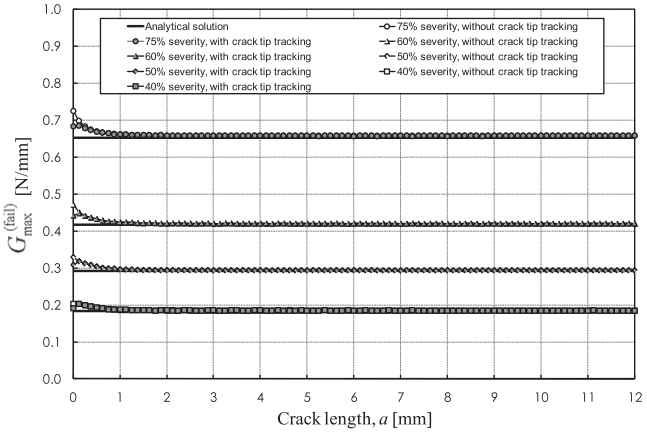

Fig. 14. Numerical and analytical strain energy release rates versus crack length for cut-ply tests.

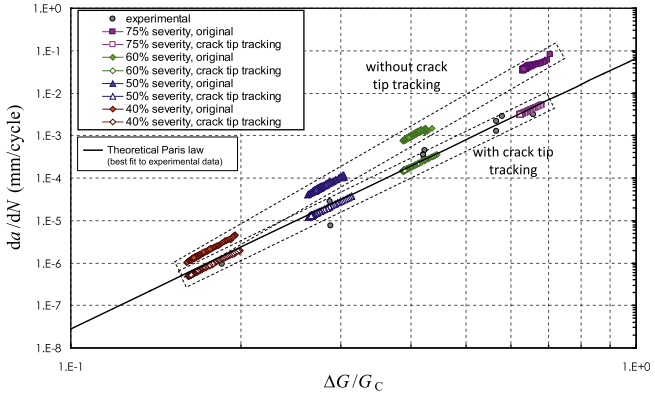

Fig. 15. Experimental and numerical Paris curves for cut-ply specimens, R-ratio 0.1.

The use of a crack tip tracking algorithm with the instantaneous strain energy release rate $G_{max}^{(inst)}$ will only provide accurate results if the mesh is fine enough so that the cohesive zone spans several elements. For coarse meshes the extraction of strain energy release rates becomes the main source of inaccuracy. This is addressed by the use of the nonlocal value $G_{max}^{(NL)}$ as illustrated in the next Section.

4.2. Circular delamination benchmark

In order to illustrate the three-dimensional aspects of the proposed formulation a circular delamination problem was investigated. This was based on the NAFEMS benchmark for circular delamination (Davies, 2002) which was here extended to the analysis of fatigue loading. This benchmark was chosen mainly for its simplicity and the availability of a closed-form analytical solution for the strain energy release rate.

In the NAFEMS benchmark a circular composite plate with simply-supported edges is loaded centrally so that a circular delamination grows radially along the mid plane which may contain a small starter crack. Because the layup is quasi-isotropic (i.e. the ply orientations are given by $[-45/90/45/0]_{xS}$ for x sub-laminates), the in-plane properties can be homogenised to make the analysis axisymmetric. A simplified analytical solution for the critical load for delamination P_c was given by Davies and Zhang (1995),

$$P_c^2 = \frac{8\pi^2 E(2h)^3}{9(1-\nu^2)}, \tag{24}$$

where h is the total plate thickness and E and ν are the isotropic elastic constants for the equivalent material properties. This

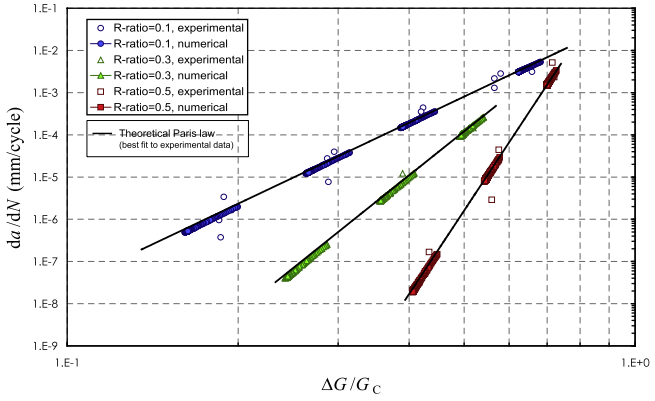

Fig. 16. Experimental and numerical Paris curves for cut-ply specimens with various R-ratios (crack tip tracking formulation, $G_{max} = G_{max}^{(inst)}$).

Table 4
Homogenised isotropic properties for T800/924 laminates.

E [GPa]	ν	σ_{II}^{max} [MPa]	G_{IIC} [N mm^{-1}]
60	0.3	57	0.8

solution was derived assuming axisymmetry and neglecting geometric nonlinearity, so it applies only to cases where deflections are small.

In the present work the plate is assumed to have a radius of 100 mm and a total thickness of 4 mm which, as will be shown later, will require geometrically nonlinear analyses. The material properties for the T800/924 carbon/epoxy material provided in the benchmark are summarised in Table 4. As for the cut-ply specimens, only mode-II properties were required due to the single-mode nature of the crack growth.

Three-dimensional quarter models were used for the cohesive element analyses as shown in Fig. 17. The laminate was modelled using hexahedral continuum elements with selective-reduced integration. Two different mesh topologies were employed. *Grid* meshes, shown in Fig. 17a, were built using elements of constant dimensions forming a regular grid, while *radial* meshes, Fig. 17b, consisted of concentric rows of elements dividing the quarter plate into 32 sectors. Six elements were used through the thickness in all cases, and a plane of cohesive elements was inserted along the mid surface. Different mesh refinements were obtained by varying the *characteristic length* of the mesh, which represents the grid spacing for grid meshes and the radial spacing between elements for radial meshes. Three levels of mesh refinement were adopted, namely:

- *coarse* mesh: 1 mm characteristic length;
- *medium* refinement: 0.5 mm characteristic length;
- *fine* mesh: 0.25 mm characteristic length.

For static loading simulations a circular pre-crack of 10 mm radius was modelled via the introduction of a plane of contact with zero friction. No pre-cracks were used in fatigue simulations in order to allow the mapping of strain energy release rates along the whole plate.

Because the analytical solution in Eq. (24) is not valid for large displacements, two-dimensional axisymmetric analyses were conducted in order to provide a reference for comparison with the three-dimensional models. The software Abaqus/Standard was used to solve all axisymmetric problems and a typical mesh is shown in Fig. 18. Bilinear axisymmetric elements with incompatible

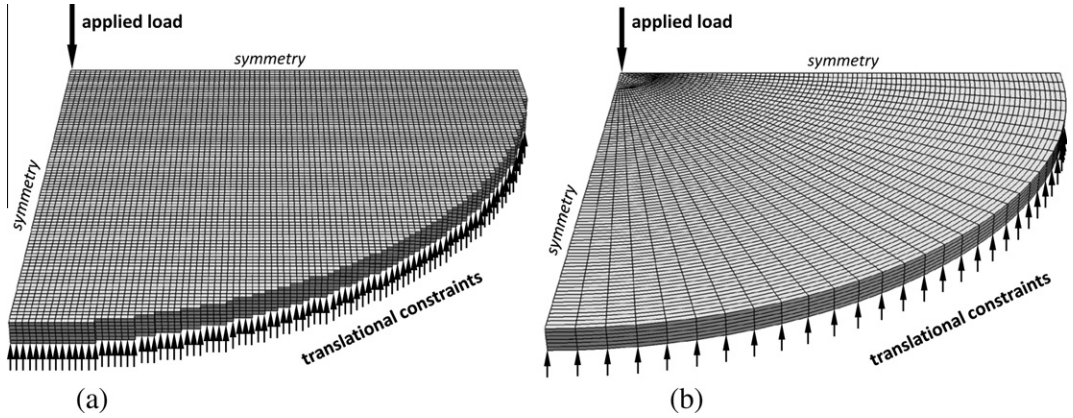

Fig. 17. Finite element meshes for the analysis of circular delamination: (a) grid mesh and (b) radial mesh.

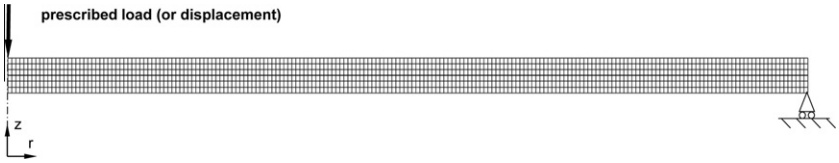

Fig. 18. 2D axisymmetric model of the circular delamination benchmark (medium refinement).

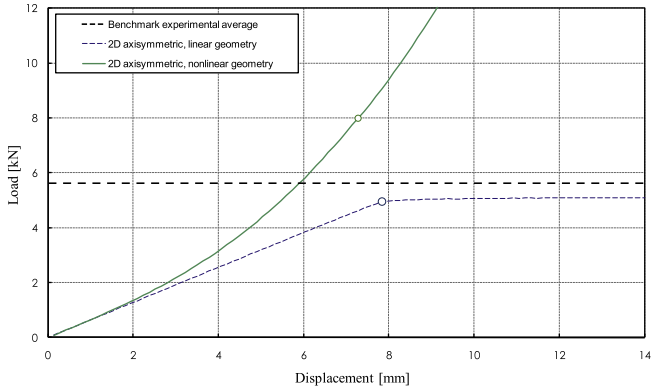

Fig. 19. Load–displacement curves for the circular delamination benchmark using axisymmetric models with and without geometrical nonlinearities (symbols mark the start of delamination propagation).

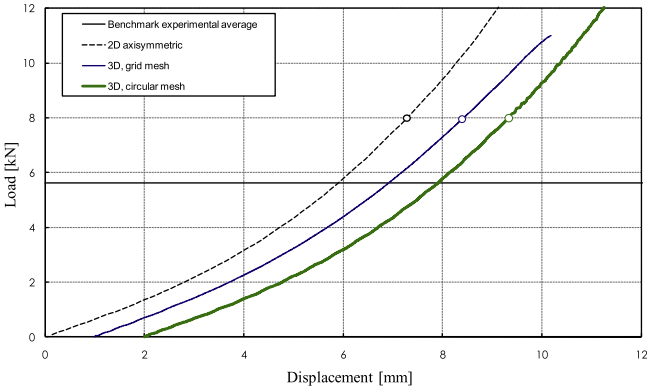

Fig. 20. Load–displacement curves for the circular delamination benchmark using axisymmetric and three-dimensional models (curves offset for clarity, symbols mark the start of delamination propagation).

modes (type CAX4I) were used to model the laminate and different strategies were adopted to model the interface. Quasi-static loading tests were analysed using built-in axisymmetric cohesive elements (type COHAX4), while the fatigue analyses were performed by applying the classical Virtual Crack Closure Technique (VCCT) (Rybicki and Kanninen, 1977). In the latter the interface was modelled using multi-point constraints and series of separate static analyses were performed with increasing delamination radii. The VCCT equations for the extraction of strain energy release rate were then applied via a Python script written for the software Abaqus/CAE.

4.2.1. Quasi-static loading

The NAFEMS benchmark assumes small displacements and hence the delamination load is not dependent on plate radius or pre-crack radius (Davies, 2002). A series of quasi-static analyses was performed using axisymmetric and full three-dimensional models in order to investigate this assumption.

Fig. 19 shows the load–displacement traces for axisymmetric models assuming either geometrical linearity or nonlinearity. It can be seen that very different results are obtained depending on this assumption. Only the linear model predicts delamination loads comparable with the benchmark solution. When geometrical nonlinearity is taken into account, the load for delamination initiation is no longer independent of pre-crack radius. For a pre-crack of 10 mm radius a considerably higher delamination load was obtained as compared with the analytical solution. One should note however that the benchmark solution could be reproduced if a smaller pre-crack were used.

The different mesh topologies for three-dimensional LS-Dyna models (grid and radial meshes) are compared with the geometrically-nonlinear axisymmetric analysis in Fig. 20. Excellent agreement was observed between the three models in terms of plate stiffness and load for delamination initiation. However, the numerical delamination loads with a pre-crack of 10 mm radius were again consistently higher than the analytical solution.

4.2.2. Fatigue loading

Cohesive analyses of fatigue delamination propagation were conducted on the three-dimensional models using the loading envelope approach described in Section 2.2 for an R-ratio of 0.1. All fatigue analyses were performed without a pre-crack in order to allow the mapping of strain energy release rates along the whole plate. Reference failure loads were obtained first by analysing the same meshes under quasi-static loading. Load envelopes for a severity ratio of 80% were then calculated based on these numerical results.

In order to verify the computation of effective element lengths, tests were conducted with a modified version of the code which enforced a constant crack growth rate da/dN instead of a Paris-law fatigue degradation. In this way the delamination growth rate was solely dependent on the computed effective element lengths. An arbitrary growth rate of 10^{-4} mm/cycle was chosen so that a delamination starting at the centre of the plate should reach the edges in about 10^6 load cycles.

Fig. 21 compares the contours of cycles to failure for the grid mesh of medium refinement assuming a constant element length and an automatic computation of effective element lengths. The use of a constant l_e resulted in a delamination pattern which is clearly not circular, Fig. 21a, revealing a strong mesh bias. In this case the delamination growth was only predicted correctly along the two directions which are parallel to the grid pattern. For other directions the crack growth rate was under-estimated showing that the approach is non-conservative. Results for the same mesh analysed with the automatic computation of l_e are shown in Fig. 21b. The delamination pattern in this case was closer to being circular and the delamination radius was not under-estimated in any direction. On the contrary, some over-estimation of the growth rate was observed as a consequence of the conservative nature of the computation of effective element lengths.

Similar tests with constant da/dN were also performed on a grid mesh with an in-plane element aspect ratio of four, and results are shown in Fig. 22. The assumption of a constant element length resulted in clear mesh bias as the delamination growth rate was higher in the direction where elements are longer, Fig. 22a. The computation of effective element lengths produced considerably better results as shown in Fig. 22b. The average effective element lengths were output for post-processing and the results for both aspect ratios are shown in Fig. 23. It can be seen that the algorithm computes the effective lengths correctly for most of the plate, with small deviations only near the edges where boundary conditions had been enforced.

The circular delamination benchmark was also analysed with the complete fatigue degradation model described in Section 2.2. Only grid meshes were used in this study, with a load severity of

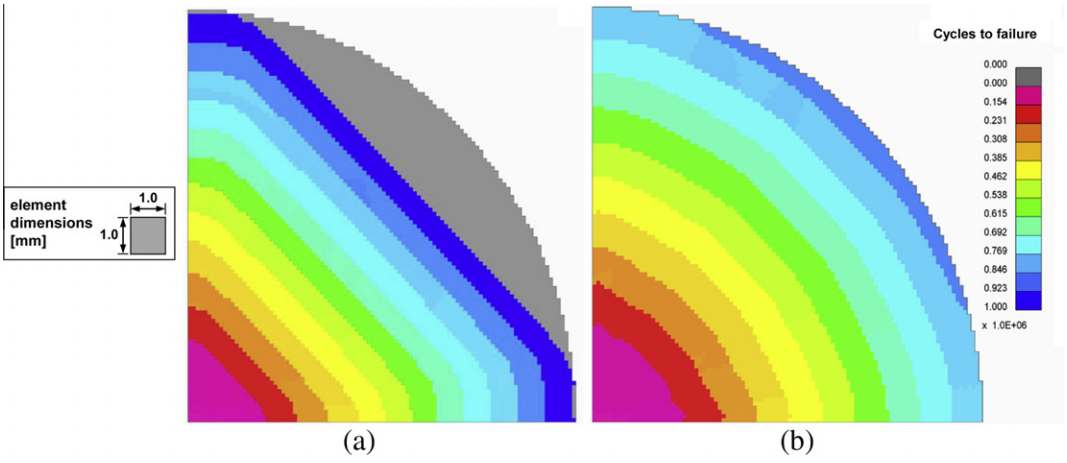

Fig. 21. Predicted contours of cycles to failure for constant da/dN simulations with a grid mesh of aspect ratio 1, (a) with fixed element length and (b) with the computation of effective element lengths.

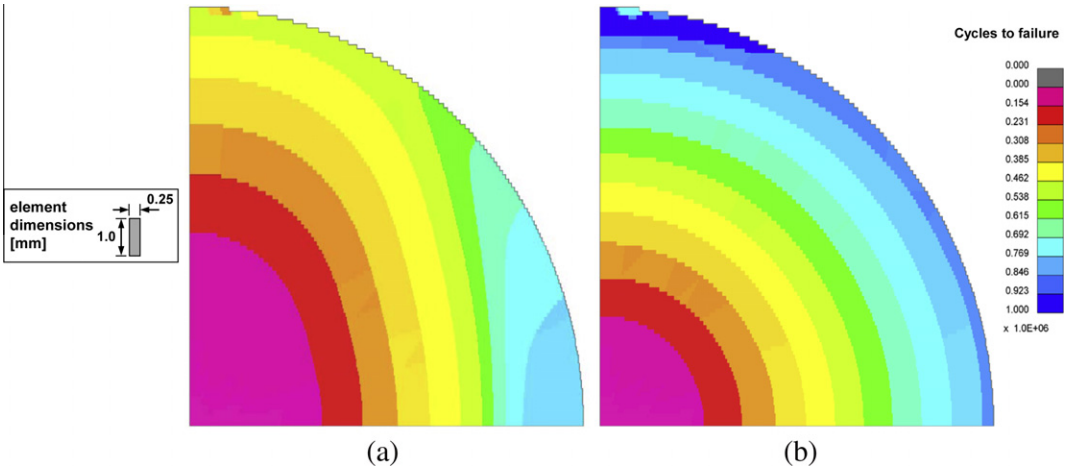

Fig. 22. Predicted contours of cycles to failure for constant da/dN simulations with a grid mesh of aspect ratio 4; (a) with fixed element length and (b) with the computation of effective element lengths.

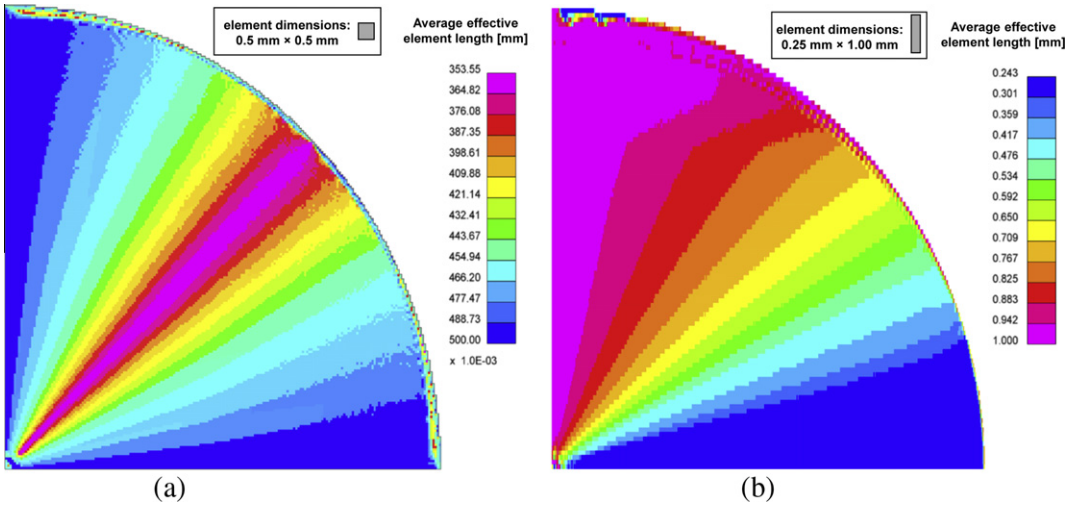

Fig. 23. Average effective element lengths on different grid meshes; (a) aspect ratio 1 and (b) aspect ratio 4.

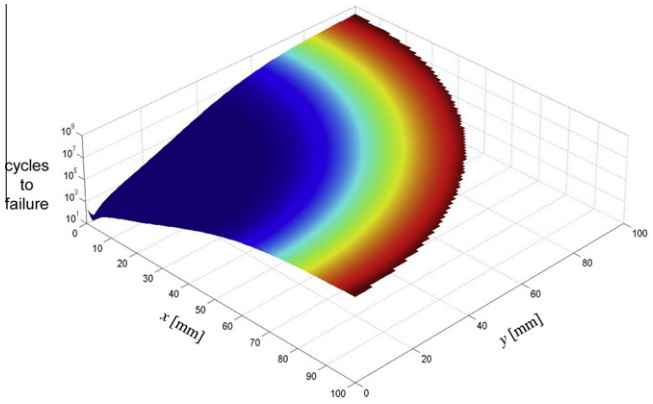

Fig. 24. Contour of cycles to failure for the circular benchmark at 80% severity (grid mesh, medium refinement).

80% and an R-ratio of 0.1 being applied in all cases. In the absence of fatigue data for the T800/924 material, it was assumed that its mode-II Paris coefficients were identical to that of the IM7/8552 material (Table 3). It should be noted that the actual values of the Paris coefficients are not important in this study since we investigate the ability of each model to reproduce the input Paris law.

Because the geometrical nonlinearities are not negligible in this case, for a constant load amplitude the strain energy release rate decreased rapidly with increasing delamination radius. Therefore in load-controlled fatigue simulations the crack growth rate also decreased very rapidly as the delamination grew away from the centre of the plate. Fig. 24 shows the number of cycles to failure for the grid mesh with medium refinement where a nearly-exponential dependency on delamination radius is observed.

In order to optimise CPU usage, an exponentially-increasing load frequency was used for the circular delamination benchmark. This frequency was given by,

$$f(t) = f_0 \cdot c_0^{(t-t_{\text{start}})c_1} \tag{25}$$

for any time $t > t_{\text{start}}$ where t_{start} is the pseudo-time at the start of the fatigue degradation step, and f_0, c_0 and c_1 are user-defined parameters describing the evolution of frequency with pseudo-time. The aim was to provide a nearly constant number of time increments for the fatigue degradation of any cohesive element in the model despite this rapidly-decelerating crack growth. A number of test runs were performed to determine which parameters would result in about 1000 fatigue time steps for every element at each load level. For 80% severity and an R-ratio of 0.1 a good combination was found to be $f_0 = 10^4$, $c_0 = 100$ and $c_1 = 2$. It should be noted that the crack growth rate will not be sensitive to the frequency

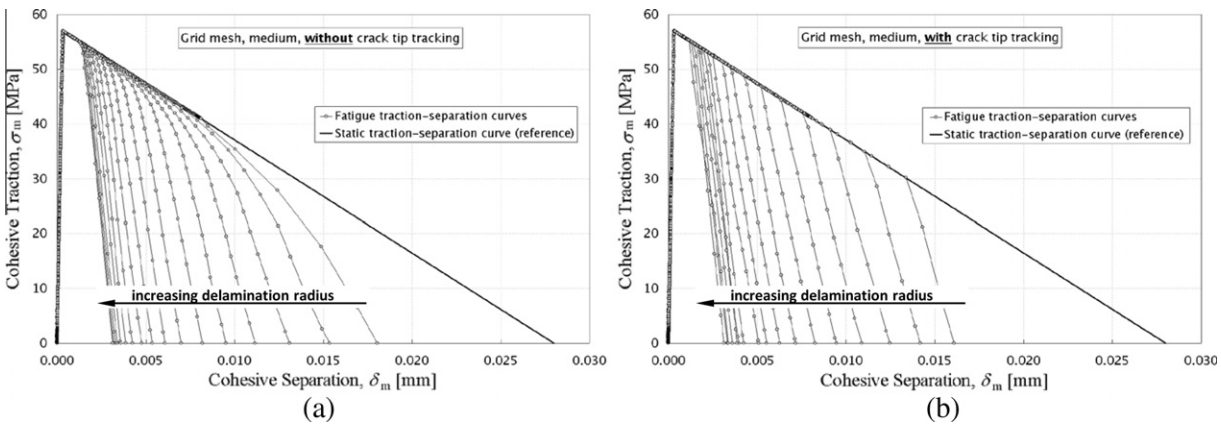

Fig. 25. Traction-separation histories for the circular delamination model (a) without and (b) with crack tip tracking (grid mesh, medium refinement).

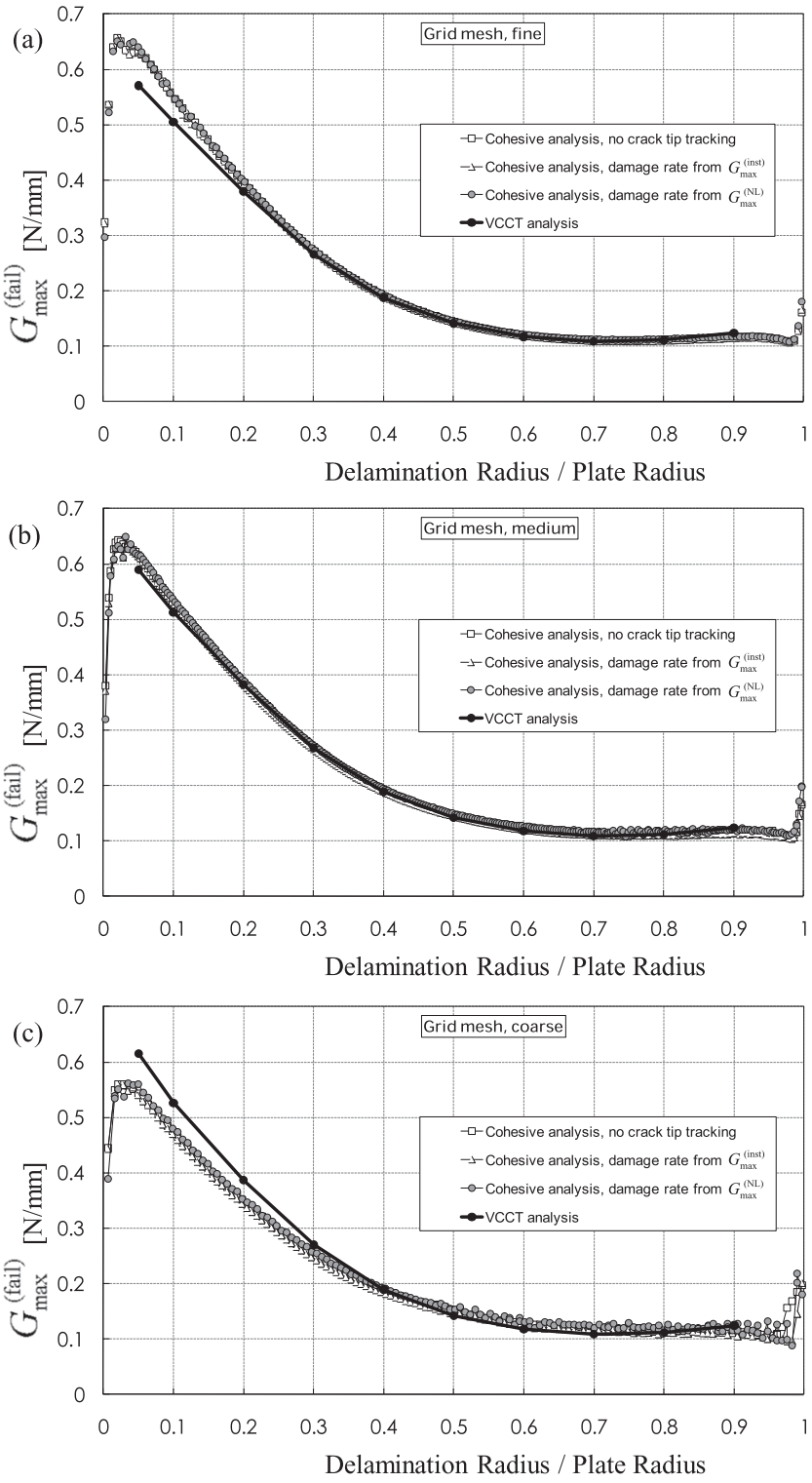

Fig. 26. Final strain energy release rate versus delamination radius for VCCT and cohesive element analyses using different mesh refinements: (a) fine, (b) medium and (c) coarse.

as long as the number of fatigue degradation time steps is not excessively small.

Circular delamination analyses were performed using the three levels of mesh refinement described earlier, as well as the three available options for the computation of damage rate, namely:

(i) no crack tip tracking, damage rate based on $G_{max}^{(inst)}$,

(ii) with crack tip tracking, damage rate based on $G_{max}^{(inst)}$,

(iii) with crack tip tracking, damage rate based on $G_{max}^{(NL)}$.

Traction and displacement data were sampled from cohesive elements at every 4 mm along the path of the fatigue crack and typical traction-separation curves are presented in Fig. 25 (grid mesh with medium refinement). The reduction in strain energy

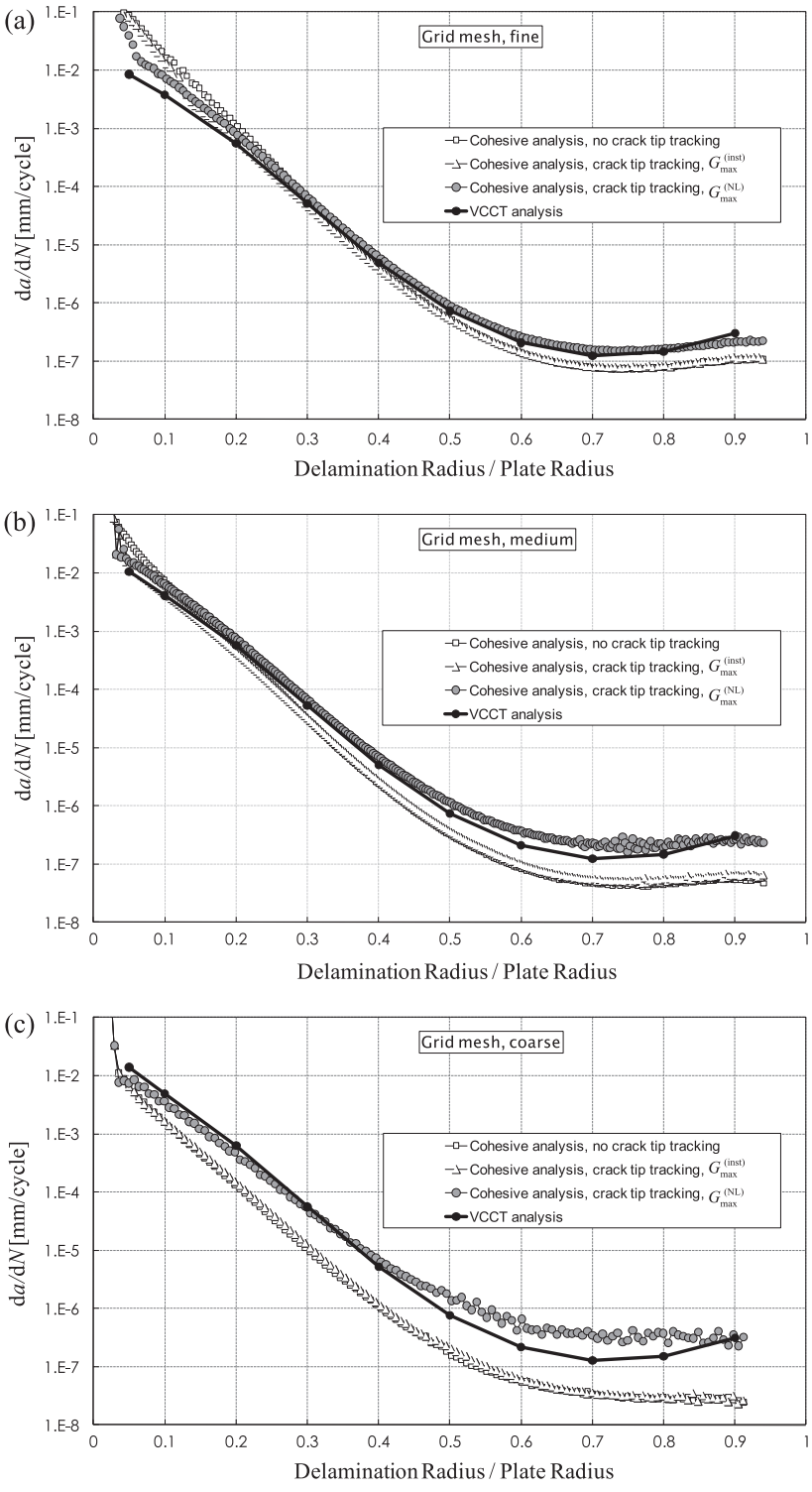

Fig. 27. Delamination growth rate versus delamination radius for VCCT and cohesive element analyses using different mesh refinements: (a) fine, (b) medium and (c) coarse.

release rate with increasing delamination radius is obvious in both graphs. Differences can be observed in the traction-separation behaviour with and without the crack tip tracking algorithm, Fig. 25a and b respectively, especially for small delamination radii where the strain energy release rates were high and the cohesive zones were long. These differences are consistent with those observed for the cut-ply tests in Fig. 13. As the delamination propagated further away from the point of loading, the cohesive zones shortened and the differences between the two options diminished. For the limit where the cohesive zones spanned only a single element, the crack tip tracking algorithm had virtually no influence on the recorded traction-separation behaviour.

Axisymmetric VCCT analyses were also performed using the same three levels of mesh refinement as for the three-dimensional models described above. The strain energy release rates at failure, $G_{max}^{(fail)}$, obtained from each method are shown as functions of delamination radius in Fig. 26. All cohesive element formulations resulted in very similar values of $G_{max}^{(fail)}$, again showing that the

fracture energy envelope is independent of the shape of the traction-separation curves in fatigue.

The results in Fig. 26 reveal different trends with respect to mesh refinement between axisymmetric VCCT and three-dimensional cohesive element analyses, especially for small delamination radii. However, the overall agreement between the two approaches was good considering that very different FE models were used in each case.

The differences between the various fatigue modelling approaches can only be fully appreciated when the effective crack growth rates are analysed. Fig. 27 shows plots of delamination growth rate versus radius for three levels of mesh refinement. For the VCCT analysis, delamination growth rates were obtained by applying Eqs. (11) and (12) to the computed strain energy release rates.

Cohesive analyses based on the use of $G_{max}^{(inst)}$ provided similar results with or without crack tip tracking. This is because the three meshes (including the *fine* mesh) were relatively coarse when compared to the short cohesive zones observed in this benchmark. In general, the analyses based on $G_{max}^{(inst)}$ resulted in poor agreement with the VCCT and considerable under-estimation of the delamination growth rates for lager radii. The use of $G_{max}^{(inst)}$ also resulted in considerable mesh-dependency because, as explained earlier, the variation of $G_{max}^{(inst)}$ during the fatigue degradation is strongly dependent on mesh refinement. The fact that this under-estimation was worse for coarser meshes is of particular concern since coarser meshes are always desired from a practical point of view.

On the other hand, crack growth rate predictions based on the nonlocal $G_{max}^{(NL)}$ showed much better agreement with the VCCT. Reasonably good agreement was observed even with a coarse mesh, Fig. 27c, where the cohesive zone was only one element long for most of the plate. This shows that $G_{max}^{(NL)}$ provides an accurate measure of the strain energy release rate even if the cohesive zone is not well-resolved. This is possible because the energy dissipated *during* the Paris-law degradation is also taken into account in the integration of strain energy release rates, which compensates for the poor resolution of cohesive tractions and displacements at the crack tip in coarse meshes.

5. Conclusions

A novel method has been proposed for the analysis of delamination propagation under fatigue loading using cohesive elements. Accurate delamination growth rates were obtained via the introduction of nonlocal aspects in the computation of the fatigue damage rate, namely (i) the identification and tracking of delamination fronts, (ii) the estimation of the local direction of propagation and (iii) the extraction of strain energy release rates from failed elements in the wake of the delamination front. The proposed formulation eliminates the need for estimating the cohesive zone length and is therefore applicable to realistic geometries and complex loading conditions. The advantages of the method have been demonstrated via the analysis of laminates with central cut plies as well as a circular delamination benchmark under cyclic loading. Predicted delamination growth rates were shown to have weak mesh-dependency and to preserve accuracy with a slight conservatism for excessively coarse meshes.

Acknowledgements

The authors would like to acknowledge Rolls-Royce Plc. for their support of this research and for their permission to publish. Thanks also to Mike Jones at the University of Bristol for experimental data from the cut-ply tests.

References

Alfano, G., Crisfield, M.A., 2001. Finite element interface models for the delamination analysis of laminated composites: mechanical and computational issues. International Journal for Numerical Methods in Engineering 50, 1701–1736.

Allegri, G., Jones, M.I., Wisnom, M.R., Hallett, S.R., 2011. A new semi-empirical model for stress ratio effect on mode II fatigue delamination growth. Composites Part A – Applied Science and Manufacturing 42, 733–740.

Barenblatt, G., 1962. The mathematical theory of equilibrium cracks in brittle fracture. Advances in Applied Mechanics 2, 55–125.

Blanco, N., Gamstedt, E.K., Asp, L.E., Costa, J., 2004. Mixed-mode delamination growth in carbon-fibre composite laminates under cyclic loading. International Journal of Solids and Structures 41, 4219–4235.

Borg, R., Nilsson, L., Simonsson, K., 2004. Simulating DCB, ENF and MMB experiments using shell elements and a cohesive zone model. Composites Science and Technology 64, 269–278.

Camanho, P.P., Davila, C.G., de Moura, M.F., 2003. Numerical simulation of mixed-mode progressive delamination in composite materials. Journal of Composite Materials 37, 1415–1438.

Chen, J., Crisfield, M., Kinloch, A.J., Busso, E.P., Matthews, F.L., Qiu, Y., 1999. Predicting progressive delamination of composite material specimens via interface elements. Mechanics of Composite Materials and Structures 6, 301–317.

Cui, W.C., Wisnom, M.R., Jones, M., 1994. An experimental and analytical study of delamination of unidirectional specimens with cut central plies. Journal of Reinforced Plastics and Composites 13, 722–739.

Davies, G.A.O., 2002. Benchmarks for Composite Delamination. NAFEMS Ltd., Hamilton, UK.

Davies, G.A.O., Zhang, X., 1995. Impact damage prediction in carbon composite structures. International Journal of Impact Engineering 16, 149–170.

Dugdale, D.S., 1960. Yielding of steel sheets containing slits. Journal of the Mechanics and Physics of Solids 8, 100–104.

Harper, P.W., Hallett, S.R., 2008. Cohesive zone length in numerical simulations of composite delamination. Engineering Fracture Mechanics 75, 4774–4792.

Harper, P.W., Hallett, S.R., 2010. A fatigue degradation law for cohesive interface elements – development and application to composite materials. International Journal of Fatigue 32, 1774–1787.

Jiang, W.G., Hallett, S.R., Green, B.G., Wisnom, M.R., 2007. A concise interface constitutive law for analysis of delamination and splitting in composite materials and its application to scaled notched tensile specimens. International Journal for Numerical Methods in Engineering 69, 1982–1995.

Jimenez, M.A., Miravete, A., 2004. Application of the finite-element method to predict the onset of delamination growth. Journal of Composite Materials 38, 1309–1335.

Li, X., Hallett, S.R., Wisnom, M.R., 2008. Predicting the effect of through-thickness compressive stress on delamination using interface elements. Composites Part A – Applied Science and Manufacturing 39, 218–230.

Nguyen, O., Repetto, E.A., Ortiz, M., Radovitzky, R.A., 2001. A cohesive model of fatigue crack growth. International Journal of Fracture 110, 351–369.

Ortiz, M., Pandolfi, A., 1999. Finite-deformation irreversible cohesive elements for three-dimensional crack-propagation analysis. International Journal for Numerical Methods in Engineering 44, 1267–1282.

Petrossian, Z., Wisnom, M.R., 1998. Prediction of delamination initiation and growth from discontinuous plies using interface elements. Composites Part A – Applied Science and Manufacturing 29, 503–515.

Planas, J., Elices, M., 1991. Nonlinear fracture of cohesive materials. International Journal of Fracture 51, 139–157.

Robinson, P., Galvanetto, U., Tumino, D., Bellucci, G., Violeau, D., 2005. Numerical simulation of fatigue-driven delamination using interface elements. International Journal for Numerical Methods in Engineering 63, 1824–1848.

Rybicki, E.F., Kanninen, M.F., 1977. Finite-element calculation of stress intensity factors by a modified crack closure integral. Engineering Fracture Mechanics 9, 931–938.

Turon, A., Costa, J., Camanho, P.P., Davila, C.G., 2007. Simulation of delamination in composites under high-cycle fatigue. Composites Part A – Applied Science and Manufacturing 38, 2270–2282.

Turon, A., Costa, J., Camanho, P.P., Maimi, P., 2008. Analytical and numerical investigation of the length of the cohesive zone in delaminated composite materials. In: Camanho, P.P., Davila, C.G., Pinho, S.T., Remmers, J.J.C. (Eds.), Mechanical Response of Composites, vol. 10. Springer-Verlag, Berlin, pp. 77–97.

Yang, B., Mall, S., Ravi-Chandar, K., 2001. A cohesive zone model for fatigue crack growth in quasibrittle materials. International Journal of Solids and Structures 38, 3927–3944.